Supplementary Information

Ion tunnel matrix-initiated oriented attachment for highly utilized Zn anodes

Dan Deng[1,#], Kai Fu[1,#], Ruohan Yu[1], Jiao Zhu[1], Hongwei Cai[1], Xiangchen Zhang[1], Jinsong Wu[1], Wen Luo[2,*], Liqiang Mai[1,3,*]

[1]State Key Laboratory of Advanced Technology for Materials Synthesis and Processing, Wuhan University of Technology, Wuhan 430070, P. R. China.

[2]Department of Physics, School of Science, Wuhan University of Technology, Wuhan 430070, P. R. China

[3]Hubei Longzhong Laboratory, Wuhan University of Technology (Xiangyang Demonstration Zone), Xiangyang 441000, China

[#]These authors contributed equally to this work.

*Corresponding author:

E-mail address*:* luowen_1991@whut.edu.cn

E-mail address*:* mlq518@whut.edu.cn

Experimental section

Materials

The chemicals include Zinc sulfate heptahydrate ($ZnSO_4·7H_2O$, Sinopharm Chemical Reagent Co.,Ltd, 99.5%), Copper sulfate pentahydrate ($CuSO_4·5H_2O$, Sinopharm Chemical Reagent Co.,Ltd, 99.0%), Nickel sulfate hexahydrate ($NiSO_4·6H_2O$, Sinopharm Chemical Reagent Co.,Ltd, 98.5%), Manganese sulfate ($MnSO_4$, Beijing Waokai Biotechnology Co., Ltd, AR), Cerium sulfate ($Ce(SO_4)_2$, Aladdin, 99.9%), Potassium citrate ($C_6H_5K_3O_7$, Macklin, 98.0%), Potassium ferricyanide ($K_3[Fe(CN)_6]$, Aladdin, 99.5%), Zinc nitrate hexahydrate ($Zn(NO_3)_2·6H_2O$, Sinopharm Chemical Reagent Co.,Ltd, 99.0%), 2-methylimidazole ($C_4H_6N_2$, Aladdin, 98.0%), 1, 3, 5-benzenetricarboxylic acid ($C_6H_3(CO_2H)_3$, Aladdin, 98.0%), N, N-dimethylformamide (C_3H_7NO, Aladdin, 99.5%), Vanadium oxide (V_2O_5, Aladdin, 99.5%), Aniline($C_6H_5NH_2$, Aladdin, 99.5%). Carbon cloth (thickness: 0.360 mm) was adopted from Taiwan CeTech Co. Ltd.

Preparation

Preparation of PBA@CC and PBA@Ti substrates. For the typical preparation of PBA@CC substrate, 20 mmol MSO_4 solution (M = Zn, Cu, Ni, Mn or Ce) and moderate potassium citrate ($C_6H_5K_3O_7$) inhibitor were dissolved into 10 ml deionized water. 10 mmol potassium ferricyanide ($K_3[Fe(CN)_6]$) was dispersed into 10 ml deionized (DI) water and then mix with the former solution. Then a piece of carbon cloth (CC, diameter: 10 mm) was immersed into the above mixture and stirred at room temperature for 2 h. Finally, the PBA@CC substrate was rinsed with distilled water and dried at 80 ℃ overnight. PBA@Ti substrate was fabricated via the same procedure but replaced CC by Ti foil with the same diameter.

Preparation of ZIF-8@CC and Zn-BTC@CC substrates. For the preparation of ZIF-8@CC, 0.2975 g $Zn(NO_3)_2·6H_2O$ and 0.3284 g 2-methylimidazole were separately dissolved into 10 ml methanol and then mixed under stirring for 5 min. A piece of CC (diameter: 10 mm) was immersed into the stirred solution for 2 h. Finally, the ZIF-8@CC substrate was rinsed with distilled water and dried at 80 ℃ overnight. For the typical preparation of Zn-BTC@CC, 1.275 g $Zn(NO_3)_2·6H_2O$ was mixed with 0.3 g 1, 3, 5-benzenetricarboxylic acid, then dissolved into 75 ml N, N-dimethylformamide (DMF). A piece of CC was immersed into the above solution with stirring and heating in an oil bath (88℃) over 2 hours, followed by washing and drying at 80 ℃ overnight.

Synthesis of PANI-intercalated V_2O_5 (PVO) cathode. A hydrothermal method was adopted to prepare the PVO cathode materials. Typically, 0.1814 g V_2O_5 powder and 60 μl aniline was added into 30 ml DI water with stirring at room temperature. Then adjust the pH of the above solution to 3 by adding dilute HCl and stirring for 30 min. The formed dark green cloudy suspension was then

transferred to a 50 mL Teflon-lined sealed autoclave and maintained at 120℃ for 24 h. Finally, the PVO sample was rinsed with deionized water and centrifuged multiple times, and then dried at 80 ℃ overnight.

Materials Characterization

The phase structure of as-prepared materials was conducted by X-Ray Diffraction (XRD, D8 Advance, Bruker AXS GmbH). Fourier transform infrared spectroscopy (FTIR) spectra were carried out using EOSXB IR spectrometer. The morphology was demonstrated by scanning electron microscopy at an acceleration voltage of 15 kV (SEM, JEOL-7100F microscope). The spherical aberration-corrected scanning transmission electron microscopy (STEM) images and elemental mapping were collected using a CEOS probe-corrected FEI Themis TEM. The depth profiles and the 3D spatial configuration of the zinc isotope were operated by Time-of-Fight secondary ion mass spectrometry (TOF-SIMS, PHI nano TOFII Time-of-Flight SIMS).

Electrochemical measurements

Electrochemical tests of various substrates are conducted with 100 mL 2.0 M $ZnSO_4$ aqueous electrolyte in CR2032 coin cells. In the Zn plating/stripping CE measurements, a rigorous 'reservoir-free' galvanostatic protocol with 100% ZUR at each cycle was applied to asymmetrical cells. PVO cast onto CC were composed of 70 wt.% of active material, 20 wt.% Super P, and 10 wt.% of polyvinylidene fluoride (PVdF) binder. For full cell tests, Zn-plated substrate and PVO was used as anode and cathode, respectively. The loading mass of cathode material is about 2 mg cm^{-2}. Our substrate of zinc anode is composed of carbon cloth decorated by PBAs (or other MOFs), which is anode-free configuration. The thickness of carbon cloth is about 0.360 mm, and the thickness of PVO cathode electrode which casted onto CC is about 0.385 mm. The anode of the full cell with high ZUR is a Zn-plated ZnFe-PBA@CC with only 20% excess of metallic Zn electrodeposited onto a ZnFe-PBA@CC substrate. For the pouch-cell format, both the anode and cathode were charged and discharged five times in the three-electrode system before assembling. The anode of the pouch cell with high ZUR is a Zn-plated 30*30 mm ZnFe-PBA@CC with 20% excess of metallic Zn.

Isotope labelling tests

NiFe-PBA@CC was selected as the model for zinc isotope labelling tests to focus on the zinc ions embedded in the nanocavities and avoid the interference of metal nodes. Swagelok-type three-electrode cells were used to prepare samples, where NiFe-PBA@CC, activated carbon and Ag/AgCl electrode serve as the working electrode, counter electrode and reference electrode, respectively. The use of zinc sheet is avoided here to prevent hybridization of the ^{64}Zn isotope labelling electrolyte. The NiFe-PBA@CC substrate underwent low-rate galvanostatic depotassium

and zinc ion insertion procedures in normal $ZnSO_4$ solution and was marked as sample A. Then, sample A was transferred to a three-electrode Swagelok cell incorporated with $^{64}ZnSO_4$ aqueous electrolyte. The substrate was initially subjected to a single galvanostatic zinc deposition in a ^{64}Zn labelled electrolyte at 0.5 mA cm^{-2} and 0.1 mAh cm^{-2}, followed by careful pickling to remove the zinc metal so that only the PBAs inlay on the carbon cloth remained (sample B). Finally, sample A and B were investigated by TOF-SIMS analysis.

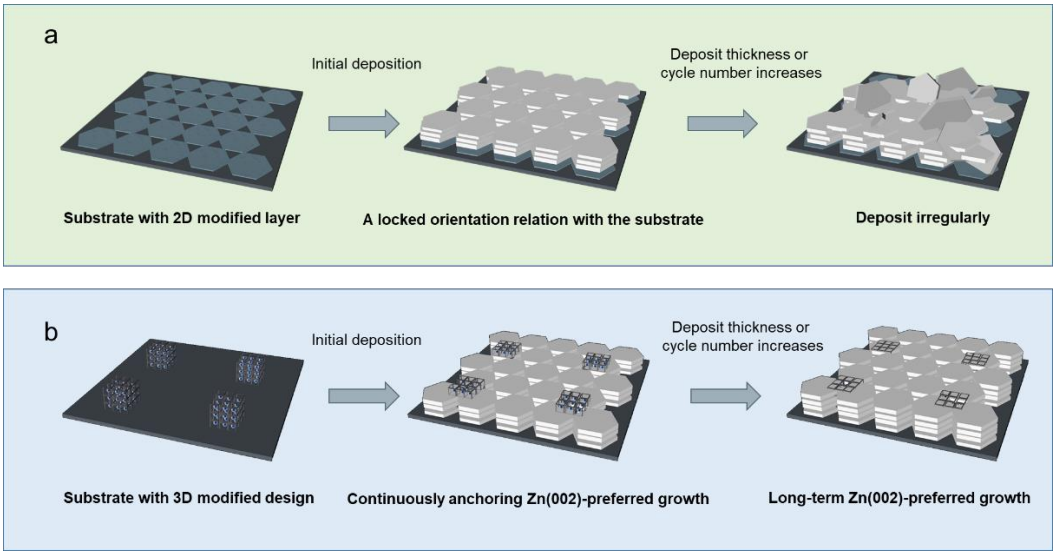

Fig. S1 Schematic of (a) Modifying the two-dimensional (2D) plane of the substrate to regulate the epitaxial deposition of Zn and (b) Modulating the morphology evolution of Zn electrodeposition in a perpendicular-to-3D view with microscopic precision

Table S1 Representative advances in substrate design for highly utilized Zn anodes.

Strategies	Methods	Performances	Ref.
2D low-lattice-mismatch interface	The low lattice mismatch between graphene and metallic Zn, and lock (002) crystallographic orientation	CE > 99.7% with 100% ZUR over 10000 cycles at 40 mA cm^{-2}.	[1]
	Anode-free Zn cell which is designed by constructing a carbon nanodiscs onto Cu foil	CE of 99.6% with 100% ZUR over 300 cycles at 1 mA cm^{-2}.	[2]
	Zn are epitaxially formed on the regularly exposed Cu (111) facets of Cu nanowire (CuNW) substrate and formed a low-mismatched Zn(002) /Cu(111) interface	Reversible zinc electroplating /stripping is achieved at 100 mA cm^{-2} for over 30000 cycles, and accumulative areal capacity up to 30 Ah cm^{-2}.	[3]
Zincophilic layer construct	A surface-alloyed nanoporous zinc (Zn_xCu_y/anode)	The symmetric cell maintains stable Zn	[4]

		stripping/plating for as long as 1900 h at 0.5 mA cm^{-2} with 37.6% ZUR.	
	ZIF-8 as host material to contain Zn^{2+} in the framework	CE ＞ 99.8% with 100% ZUR over 200 cycles at 30 mA cm^{-2}.	[5]
	A 2D antimony/antimony-zinc alloy heterostructured interface	CE of 97.8% with 100% ZUR over 550 cycles at 5 mA cm^{-2}.	[6]

Table S2 Parameters used to calculate the energy density of different battery systems

Battery system	**Electrochemical reaction equation**	**Capacity (mAh g^{-1})**	**Voltage (V)**	**Energy density (Wh kg^{-1})**
Pb-acid	Anode: $Pb+SO_4^{-2} = PbSO_4+2e^-$ Cathode: $PbO_2+ SO_4^{-2}+4H^++2e^- = PbSO_4+2H_2O$	176 158	1.9	158.5
Ni-Cd	Anode: $Cd+2OH^- = Cd(OH)_2+2e^-$ Cathode: $PbO_2+ SO_4^{-2}+4H^++2e^- = PbSO_4+2H_2O$	366 244	1.2	175.3
Ni-MH	Anode: $LaNi_5H_6+6OH^- = LaNi_5+6e^-$ Cathode: $NiOOH+ H_2O +e^- = Ni(OH)_2+OH^-$	371 244	1.3	192.2
Li-ion	Anode: $LiC_6 = 6C+Li^++e$ Cathode: $LiFePO_4+xe^-= Li_{1-x}FePO_4+2H_2O$	339 170	3.3	373.8
Zn-NiOOH	Anode: $Zn+2OH^- = Zn(OH)_2+2e^-$ Cathode: $NiOOH+H_2O+e^- = Ni(OH)_2+OH^-$	539 244	1.6	268.8 (100% ZUR) 249.9 (80 % ZUR) 38.8 (5 % ZUR)
Zn-V_2O_5	Anode: $Zn = Zn^{2+}+2e^-$ Cathode: $Zn_2V_2O_5+4e^- = V_2O_5+2Zn^{2+}$ （Based on V^{3+}-V^{5+} redox）	819 343	1.0	243.3 (100% ZUR) 225.7 (80 % ZUR) 36.6 (5 % ZUR)
Zn-MnO_2	Anode: $Zn = Zn^{2+}+2e^-$	819	1.5	264.6 (100% ZUR)

	Cathode: $Zn_{0.5}MnO_2+e^- = MnO_2+0.5Zn^{2+}$ (Based on Mn^{2+}-Mn^{3+} redox)	224		250.4 (80 % ZUR) 51.9 (5 % ZUR)
Zn-I_2	Anode: $Zn = Zn^{2+}+2e^-$ Cathode: $I_2+2e^- = 2I^-$ (Based on I^{-1}-I^0 redox)	819 211	1.3	218.0 (100% ZUR) 207.5 (80 % ZUR) 44.6 (5 % ZUR)
Zn-PVO	Anode: $Zn = Zn^{2+}+2e^-$ Cathode: $PVO+ xZn^{2+}+2xe^- = Zn_xPVO$	819 408	0.84	228.8 (100%ZUR)

Note: (a) The specific capacity is calculated from the half reaction counting the mass of all substances involved in the half-reaction to make a proper comparison between different electrodes[7]. For example, the specific capacity for graphite should be calculated as:

$$C_G = \frac{F}{6 \times M_G + M_{Li}} = \frac{96485(A \cdot s \cdot mol^{-1})}{78.95(g \cdot mol^{-1})} = 1222.10\ A \cdot s\ g^{-1} = 339.47\ mAh\ g^{-1}$$

, in which not only counting the weight of the host graphite (C_6), but also accounts for the Li involved in the reaction.

(b) The specific capacity of PVO cathode is based on the measured value at 0.1 A g^{-1} because the theoretical value is unknown.

(c) The voltage of commercial aqueous systems and Li-ion battery for calculation is the nominal voltage (plateau voltage). While the measured median discharge voltage at 0.1 A g^{-1} is used for our Zn-PVO battery to avoid overestimation of the specific energy density.

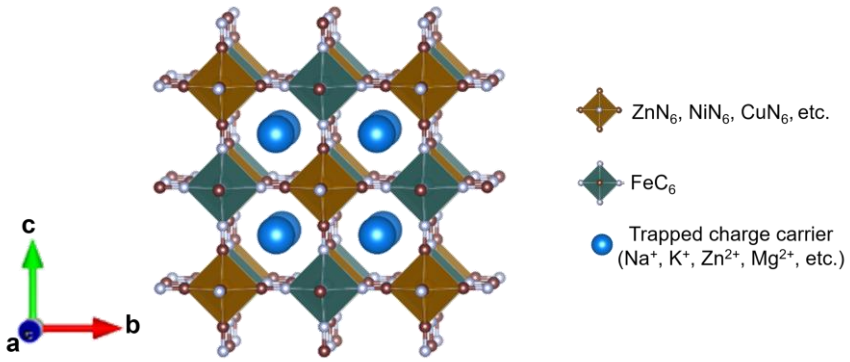

Fig. S2 3D open structure of cubic type Prussian blue analogues (PBAs) with space group of Fm-3m.

The alternating connections of M-N and Fe-C bonds through the cyanide groups build up a 3D framework filled with charge carriers. Charge carriers (such as Zn^{2+}) tend to occupy the PBA nanocavities and migrate through the 3D tunnel of PBA frameworks. PBAs are versatile ion hosts for sustainable electrochemical energy storage applications due to their open framework structure containing wide intersecting tunnels for the diffusion of various charge carrier ions. Compared with layered electrode materials, PBA promise rapid ions mobility and mild volume variation because of their double perovskite frameworks built up by Fe-C≡N-M units. The cubic type PBA can be considered an ideal zinc ion trap and tunnel matrix if its nanocavities are equally spaced at

approximately 5 Å and exhibit a small lattice misfit with the (002) plane of metallic Zn.

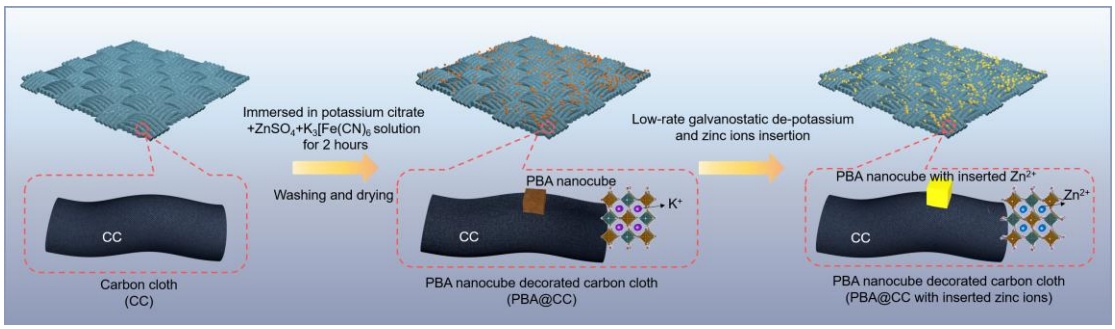

Fig. S3 Schematic illustration of the fabrication process of the ZnFe-PBA@CC with inserted zinc ions.

PBA nanocubes with high crystallinity, regular cubic morphology and narrow particle size distribution can be directly grown on a CC or Ti foil substrate via a moderate precipitation method by using potassium citrate as an inhibitor. Prior to plating/stripping tests, the PBAs rooted on the substrate underwent low-rate galvanostatic depotassium and zinc ion insertion procedures. Notably, zinc ions tend to occupy the nanocavities and migrate through the 3D tunnel of PBA frameworks at the equilibrium potential of Zn^{2+}/Zn conversion.

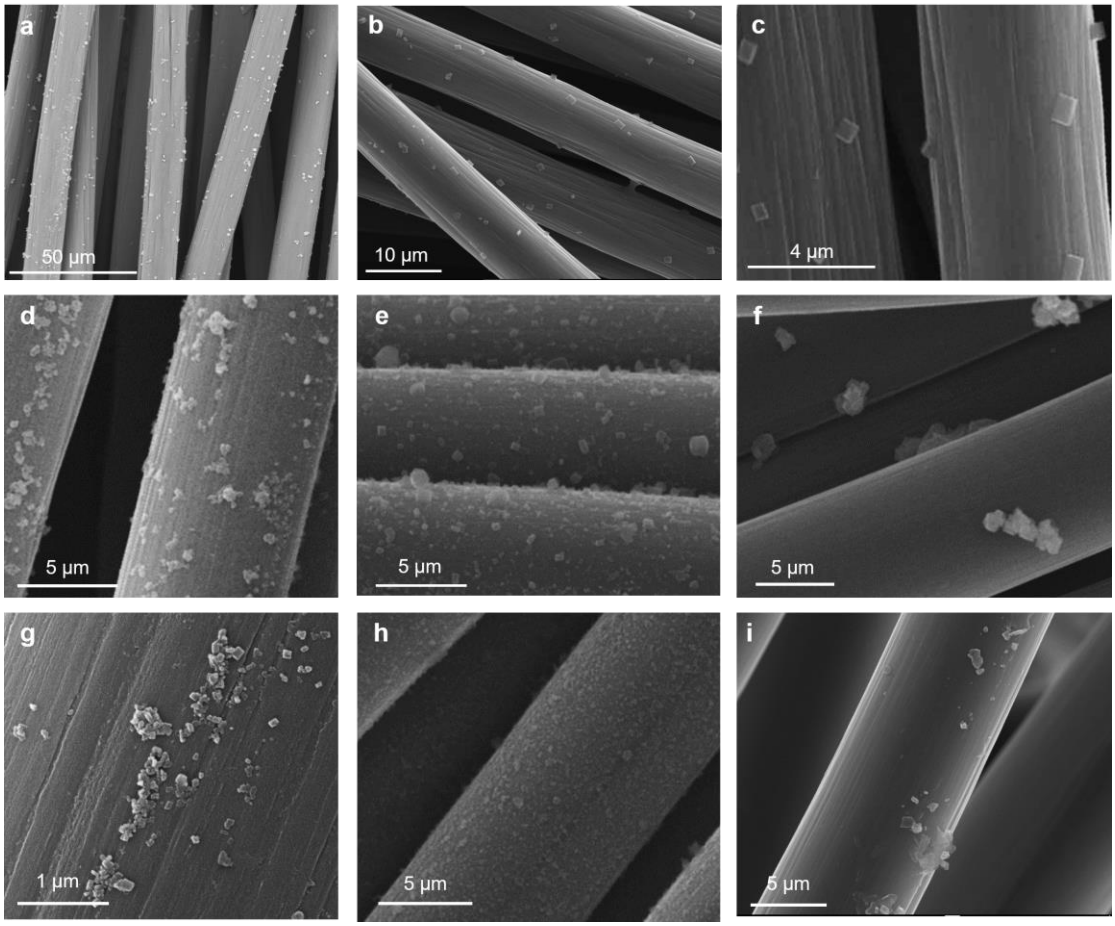

Fig. S4 SEM images of different MOFs@CC. (a-c) ZnFe-PBA@CC; (d) NiFe-PBA@CC; (e)

CuFe-PBA@CC; (f) MnFe-PBA@CC; (g) CeFe-PBA@CC; (h) ZIF-8@CC; (i) Zn-BTC@CC.

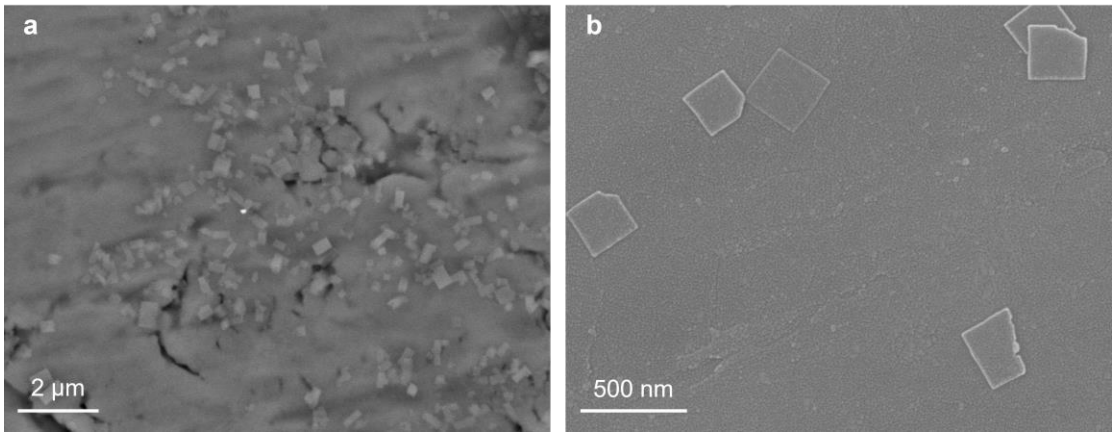

Fig. S5 (a, b) SEM images of ZnFe-PBA@Ti.

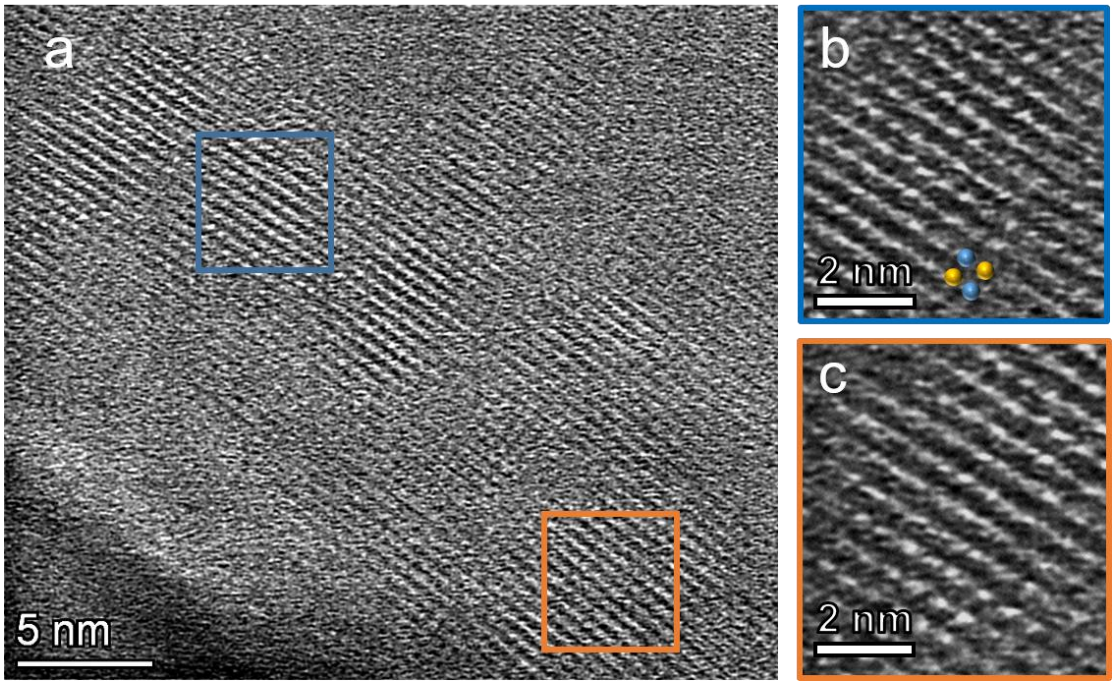

Fig. S6 (a-c) High-magnification BFTEM images of the ZnFe-PBA.

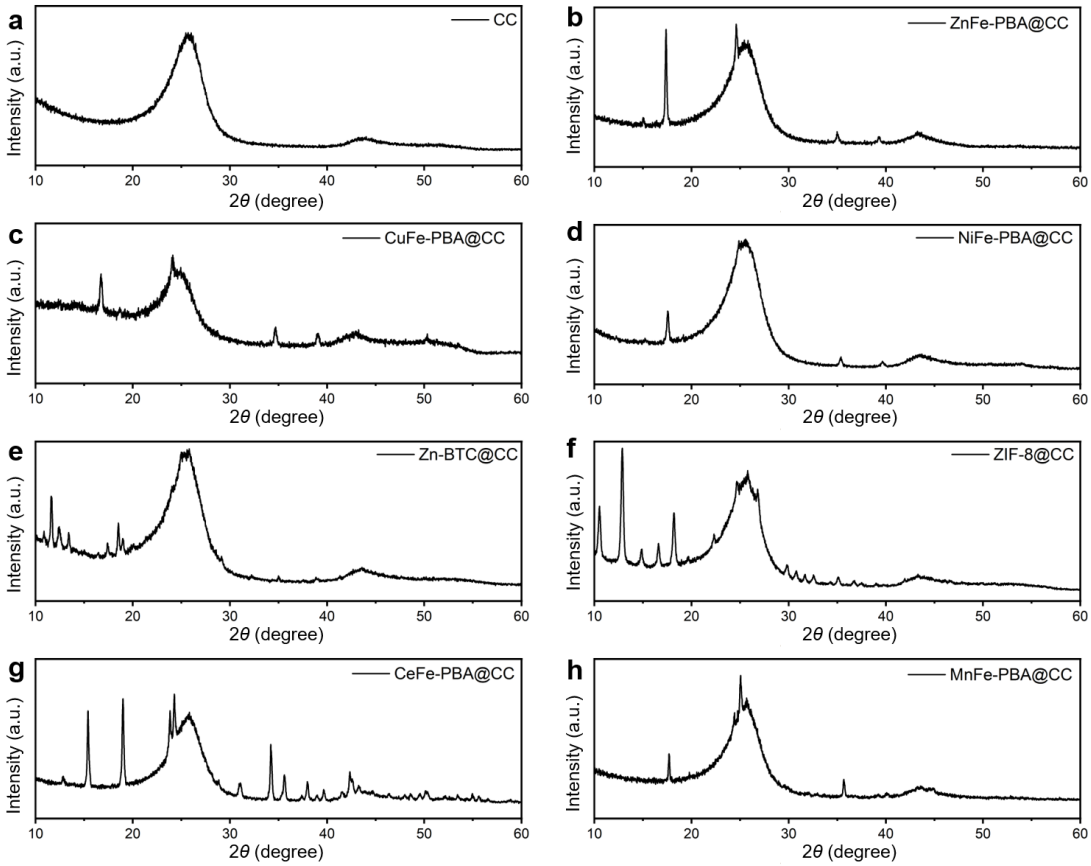

Fig. S7 XRD image of different MOFs@CC. (a) CC. (b-d) cubic-type PBA@CC. (e, f) other MOFs@CC. (g, h) non-cubic-type PBA@CC.

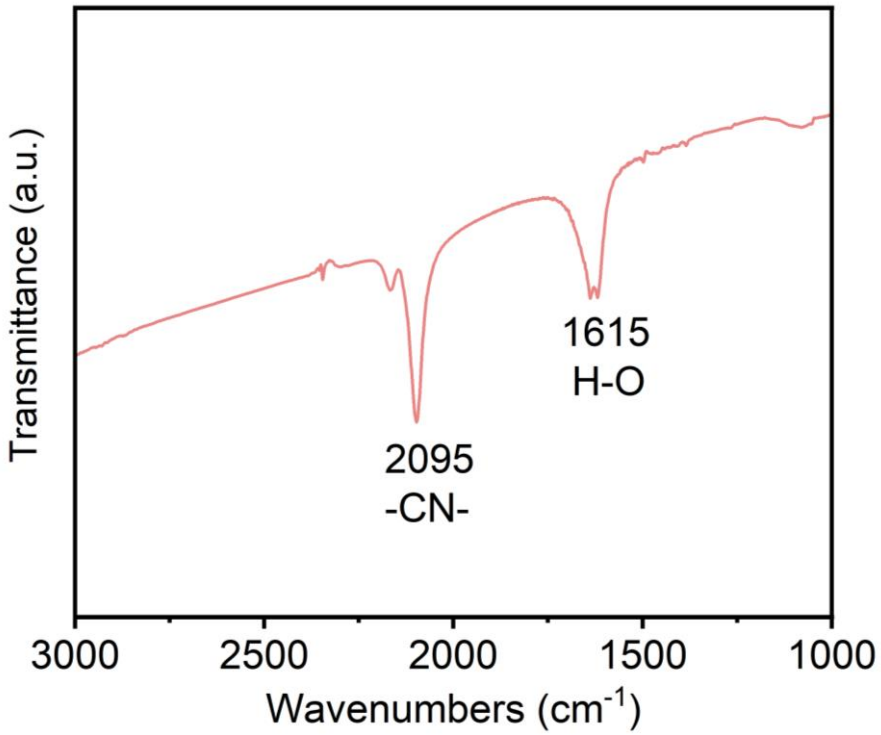

Fig. S8 FTIR spectra of ZnFe-PBA@CC substrate.

The peak at 1615 cm^{-1} ascribes to the deformation vibration mode of hydroxyl groups. The band at 2095 cm^{-1} is assigned to the C≡N vibration in the PBA frameworks, indicating the cyanide-constructed crystal structure in La-Fe PBA

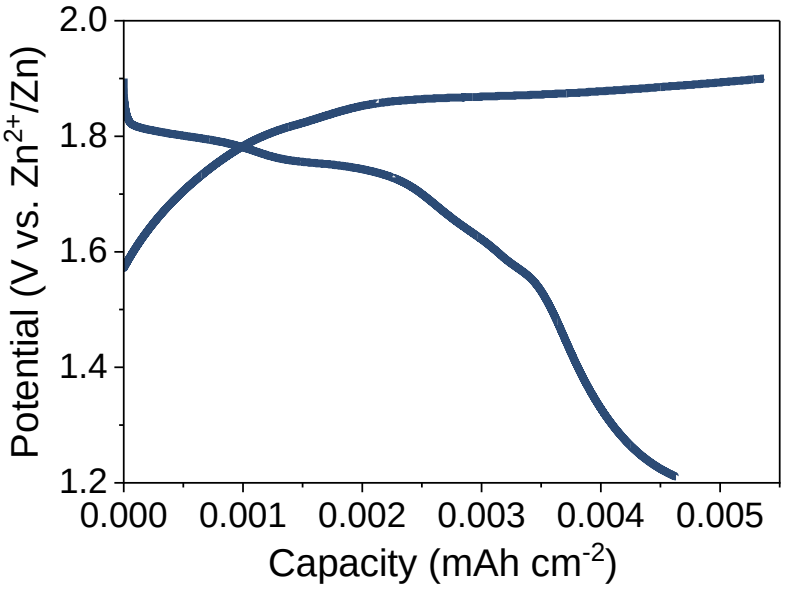

Fig. S9 The GCD curves of K^+ extraction/Zn^{2+} insertion pretreatment.

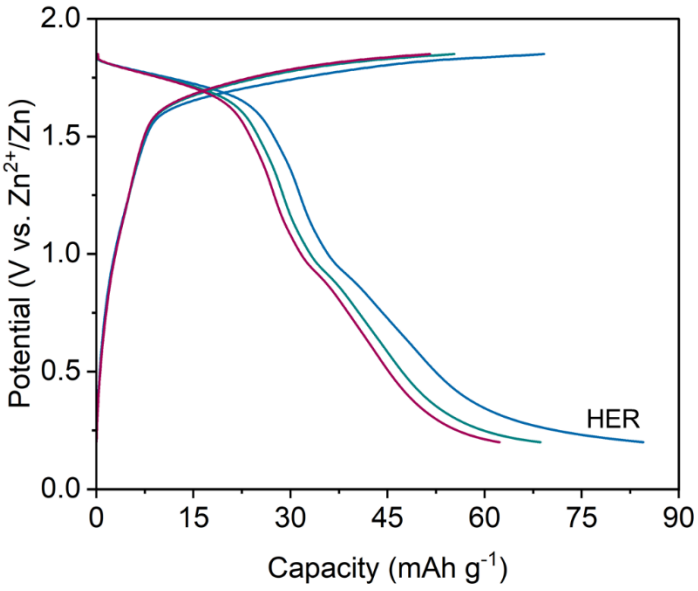

Fig. S10 The GCD curves of ZnFe-PBA electrodes for reversible Zn^{2+} storage at 0.5 mA cm^{-2}.

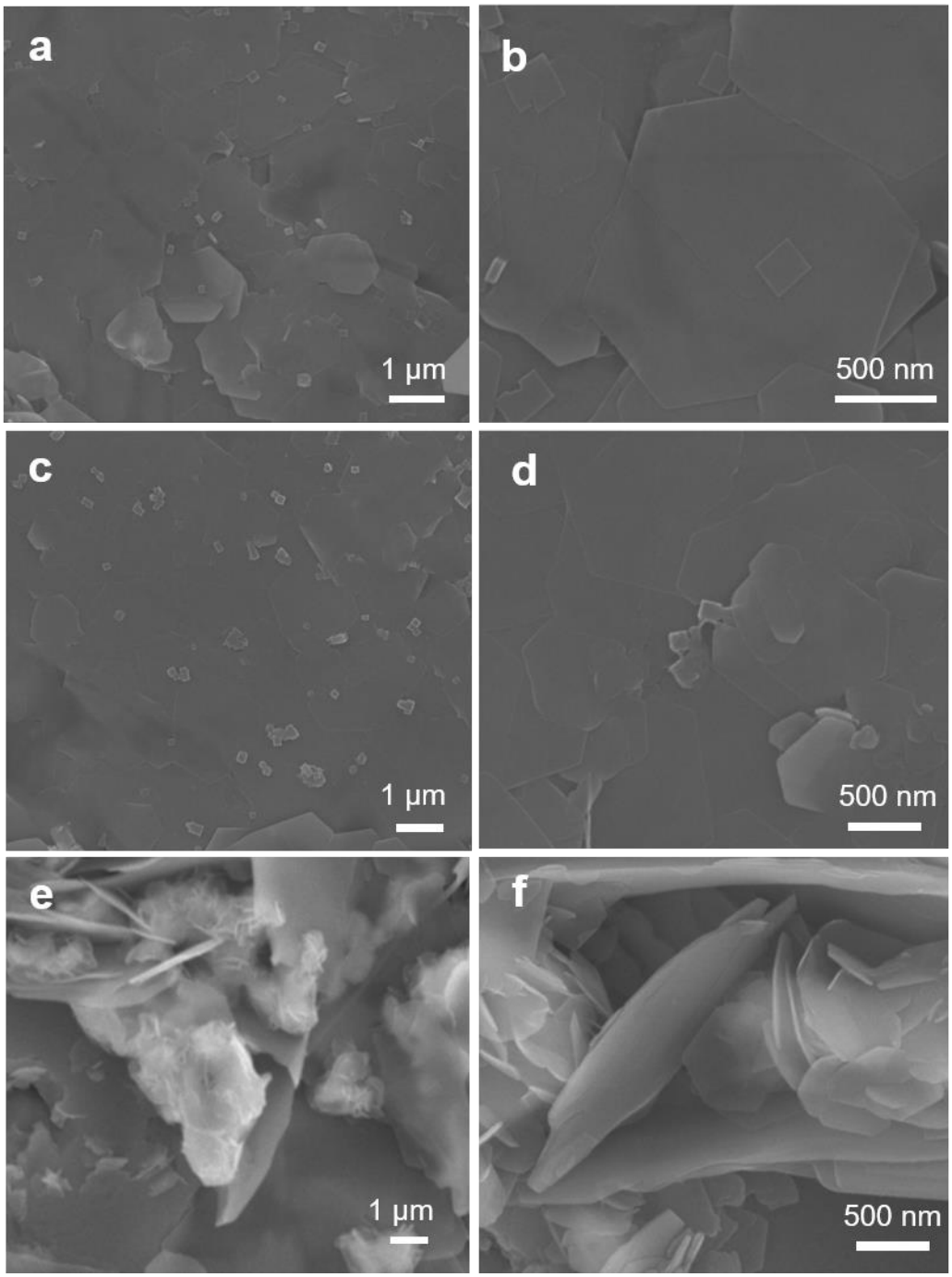

Fig. S11 SEM images of Zn-plated substrates: (a, b) ZnFe-PBA@Ti. (c, d) NiFe-PBA@Ti. (e, f) untreated Ti foil after Zn deposition at 0.5 mA cm^{-2} and 0.5 mAh cm^{-2}.

After zinc electrodeposition, scanning electron microscopy (SEM) images show a highly oriented dense hexagonal Zn deposits on the cubic-type PBA@Ti substrates with a smooth and flat surface, indicating preferred deposition of Zn (002) plane. In sharp contrast, aggressive dendritic growth was observed for untreated Ti foil.

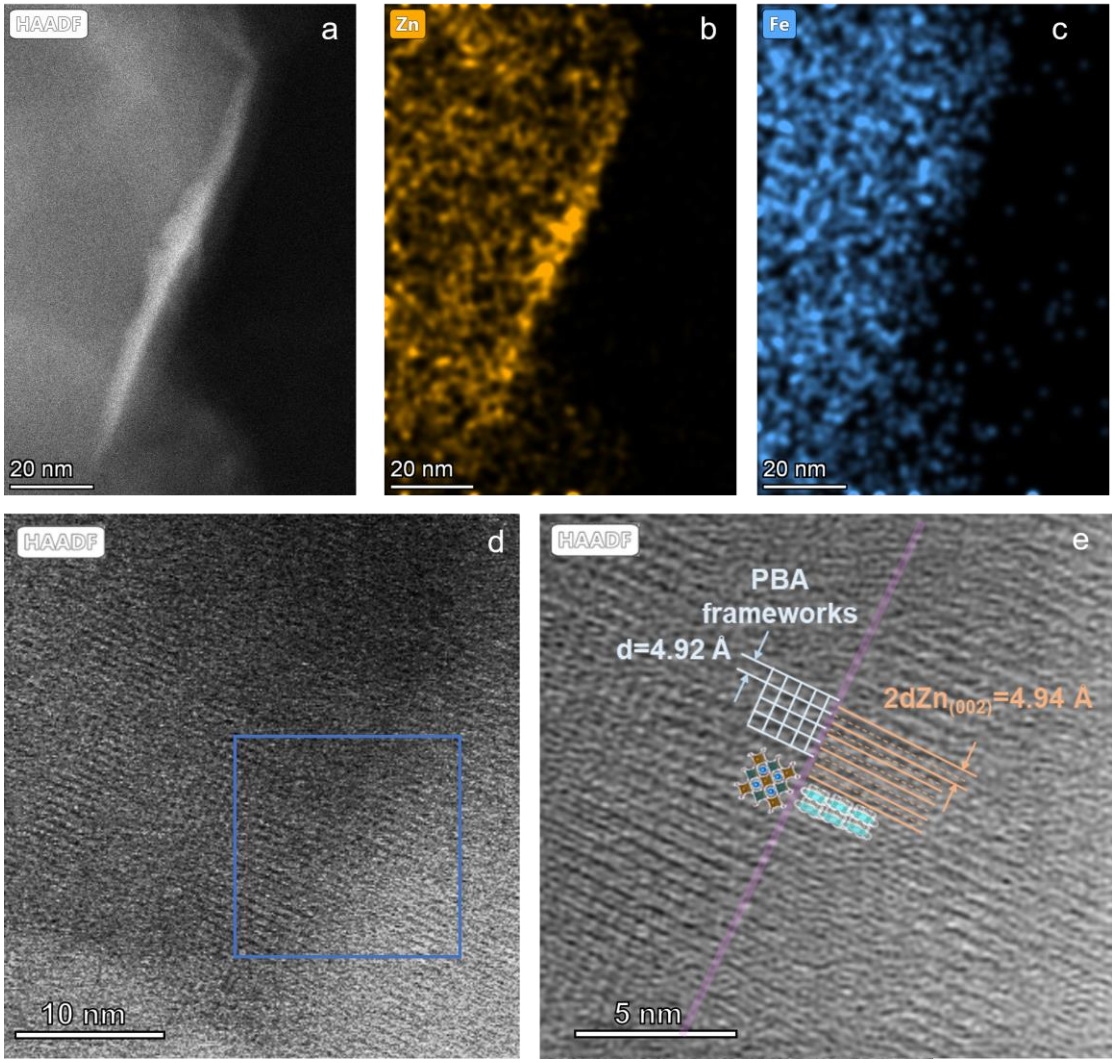

Fig. S12 High-magnification TEM images of the PBA-Zn interface

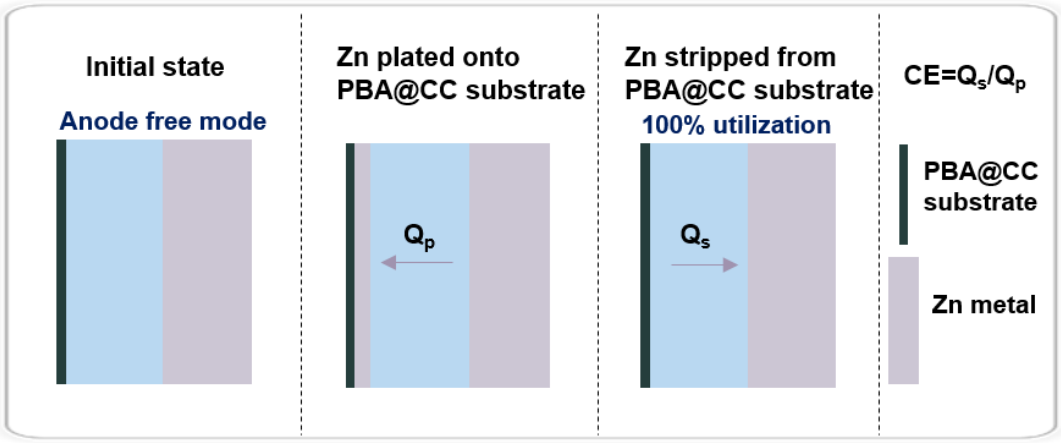

Fig. S13 A schematic of the proposed 'reservoir free' galvanostatic protocol for evaluating Zn stripping/plating CE.

A rigorous 'reservoir free' galvanostatic protocol in the configuration of substrate|Zn with 100% ZUR per cycle. Substrates that can pass this protocol would gain high confidence in being capable of supporting higher-energy-density cell formats. A fixed capacity of Zn (Qp) was plated on the substrate and stripped (Qs) during each cycle. CE is calculated using the equation in the inset.

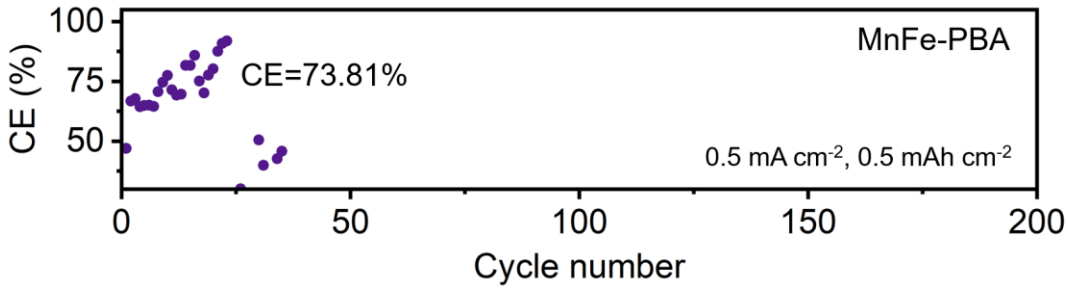

Fig. S14 Coulombic efficiency of MnFe-PBA@CC substrates at 0.5 mA cm^{-2}, 0.5 mAh cm^{-2}.

For the MnFe-PBA@CC substrate, the plating/stripping efficiency rises slightly at first and then oscillates randomly, showing a sharp decline after 22 cycles and a low average CE of 77.13%.

According previous reports, the MnFe-PBA exhibit monoclinic initial structure and experiences two two-phase transitions (monoclinic to cubic and cubic to tetragonal phases) during ion insertion. These may be the reason for its poor cycling performance.

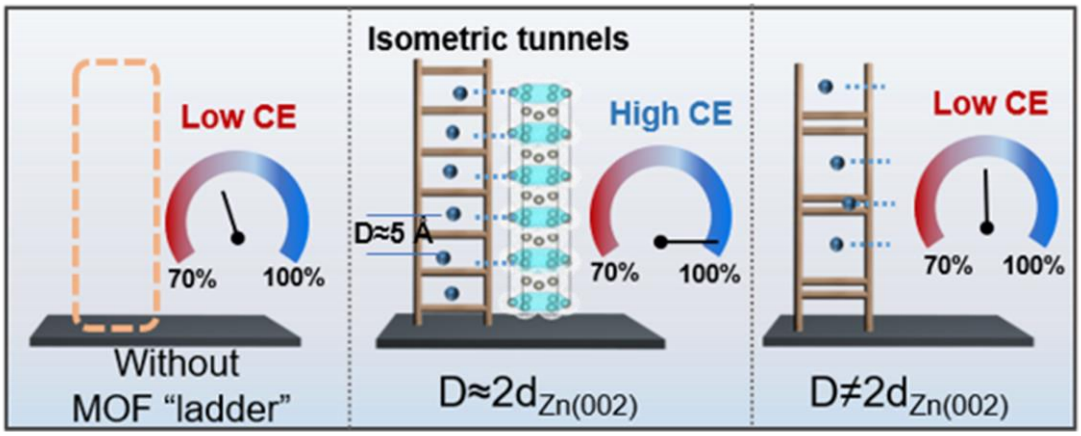

Fig. S15 Illustration of the rational screening of MOFs for highly reversible Zn plating/stripping.

Both average CE and lifetime of Zn plating/stripping can be significantly improved by introducing cubic-type PBA on CC substrate. However, once the inlaid PBA is replaced by non-cubic phase types, the effect on the enhancement of Zn plating/stripping reversibility is seriously reduced. If other typologies of MOFs are used as 'ladders', the reversibility of Zn plating/stripping on the substrate becomes quite poor and almost identical to that of untreated CC. Cubic-type PBA presented a FCC structure in space group Fm-3m with equally spaced 3D ion trap matrix. From the crystal structure point of view, cubic-type PBA is a consummate candidate for the MOF 'ladder' with fixed Zn^{2+} trapping sites because of its ~5 Å spaced cyanide-bridged architecture. The Zn^{2+} trapped by isometric ion trap functions as initial source of metallic Zn nucleation, inviting the Zn(002) preferential orientation and regulating horizontally epitaxial growth of Zn deposition. Once the spacing of the MOF 'ladder' is inappropriate and/or non-uniform in the vertical substrate direction, the reversibility of Zn plating/stripping deteriorates.

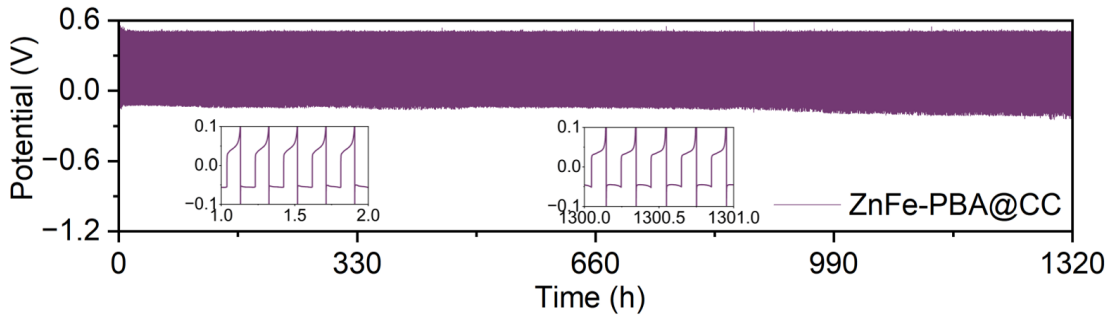

Fig. S16 Voltage profiles of Zn plating/stripping of ZnFe-PBA@CC substrates at 5 mA cm^{-2}, 0.5 mAh cm^{-2} in 2.0 M $ZnSO_4$ electrolyte.

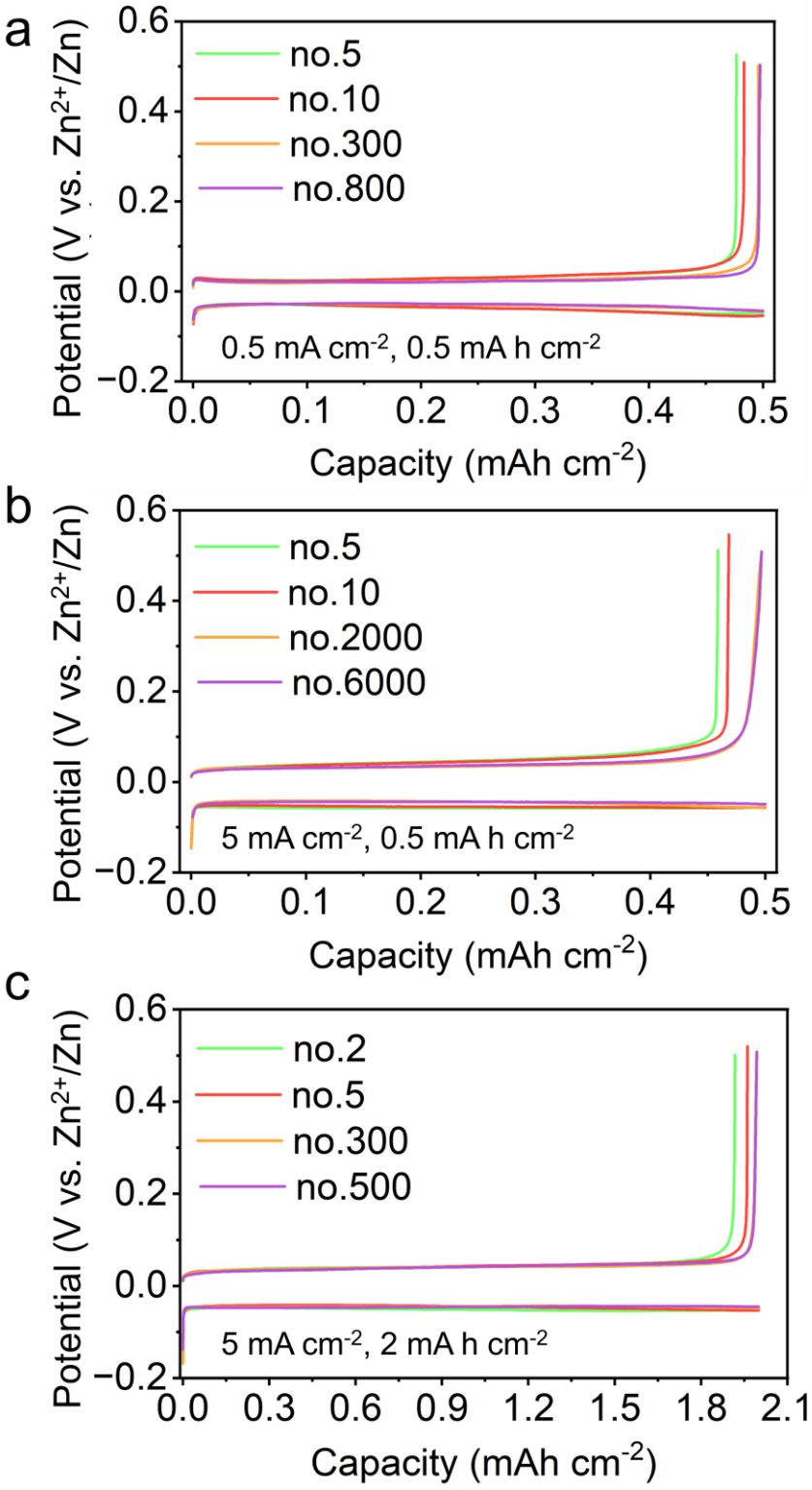

Fig. S17 Charge/discharge profiles of ZnFe-PBA@CC at (a) 0.5 mA cm^{-2}, 0.5 mA h cm^{-2}, (b) 5 mA cm^{-2}, 0.5 mA h cm^{-2}, (c) 5 mA cm^{-2}, 2 mA h cm^{-2}.

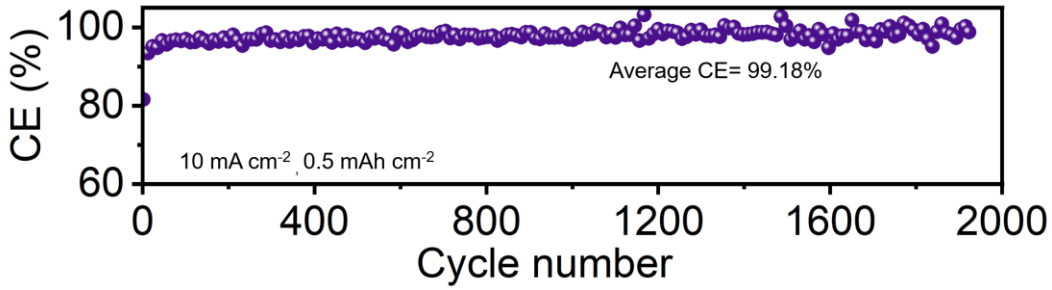

Fig. S18 Coulombic efficiency of ZnFe-PBA@CC substrates at 10 mA cm^{-2}, 0.5 mAh cm^{-2}.

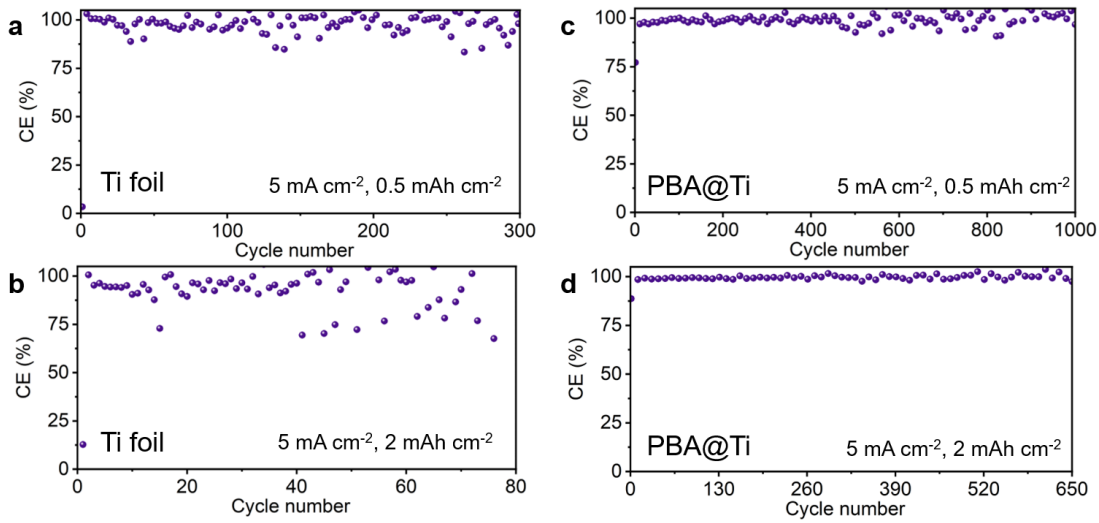

Fig. S19 Coulombic efficiency of (a-b) Ti foils and (c-d) PBA@Ti substrates at 5 mA cm^{-2} with different capacities.

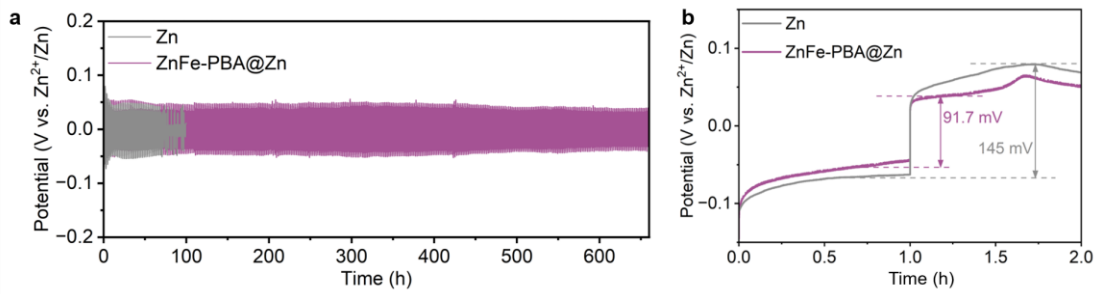

Fig. S20 (a) The cycling performance of symmetric battery of ZnFe-PBA@Zn//ZnFe-PBA@Zn and Zn//Zn was tested at 0.5 mA cm^{-2}, 0.5 mA h cm^{-2}. (b) The initial voltage curves.

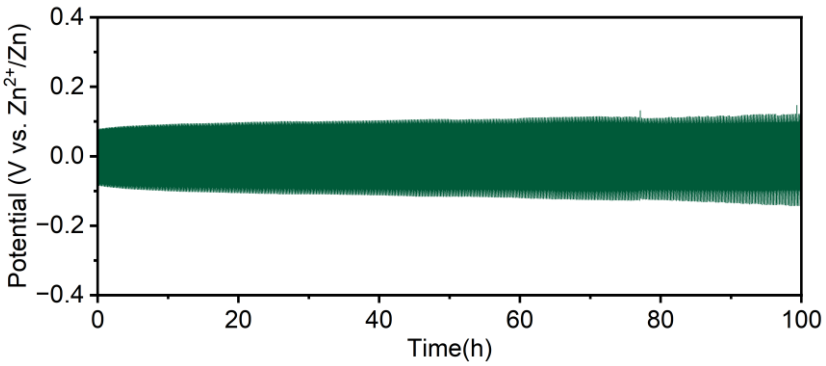

Fig. S21 The cycling performance of symmetric battery of Zn-plated ZnFe-PBA@CC//Zn-plated ZnFe-PBA@CC tested at 5 mA cm^{-2}, 0.5 mAh cm^{-2} (the ZnFe-PBA@CC electrodes was pre-deposited with a capacity of 2 mAh cm^{-2}).

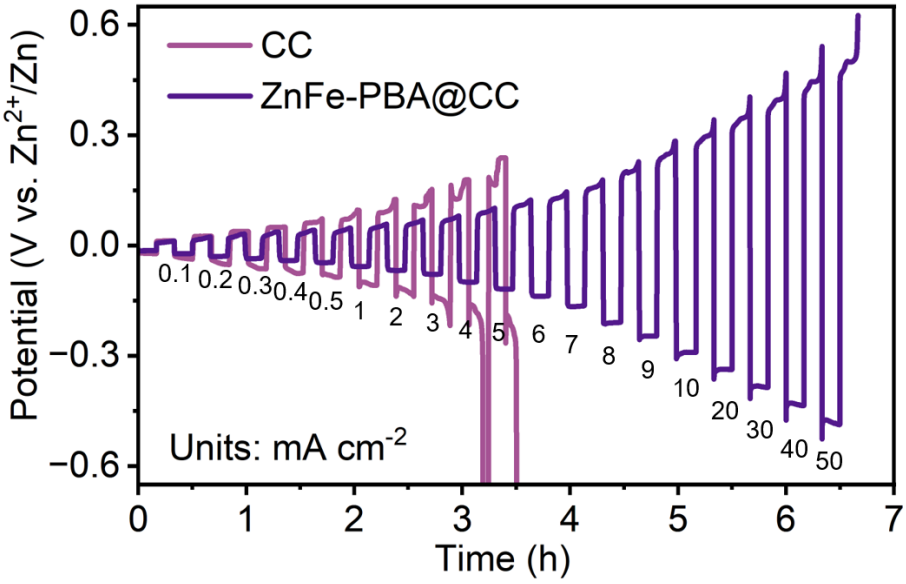

Fig. S22 Comparison of the Zn plated-ZnFe-PBA@CC//Zn-plated ZnFe-PBA@CC and the Zn plated CC//Zn-plated CC symmetric battery tested at different current densities (0.5-50 mA cm^{-2}).

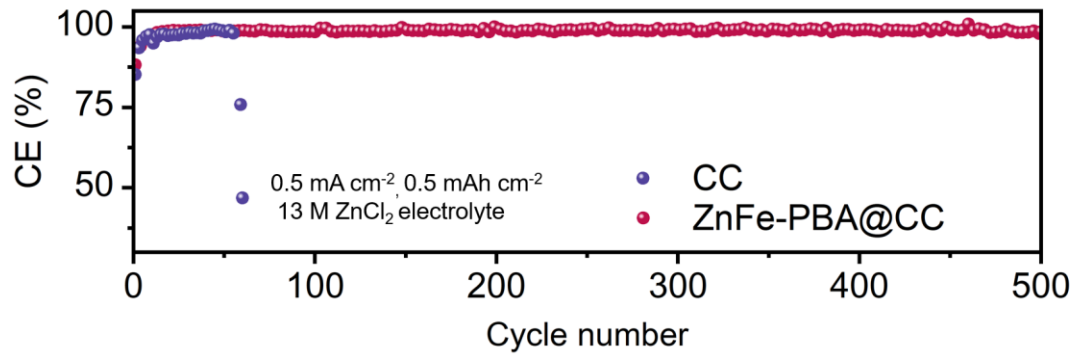

Fig. S23 Coulombic efficiency comparison of ZnFe-PBA@CC and CC substrates at 0.5 mA cm^{-2}, 0.5 mAh cm^{-2} in 13.0 M $ZnCl_2$ electrolyte.

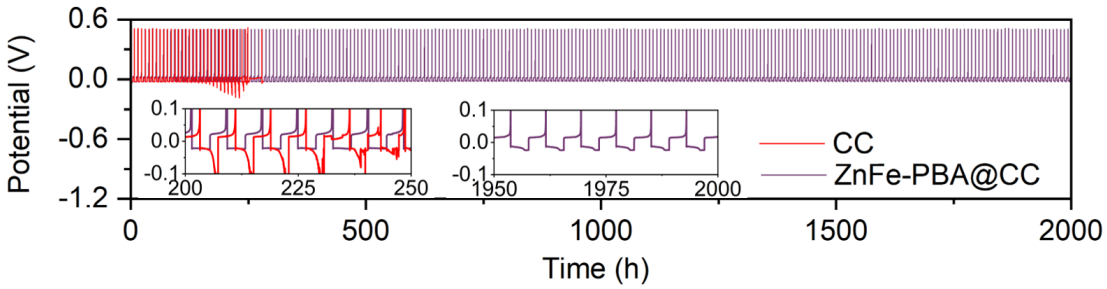

Fig. S24 Voltage profiles of Zn plating/stripping of ZnFe-PBA@CC and CC substrates at 0.5 mA cm^{-2}, 2 mAh cm^{-2} in 13.0 M $ZnCl_2$ electrolyte.

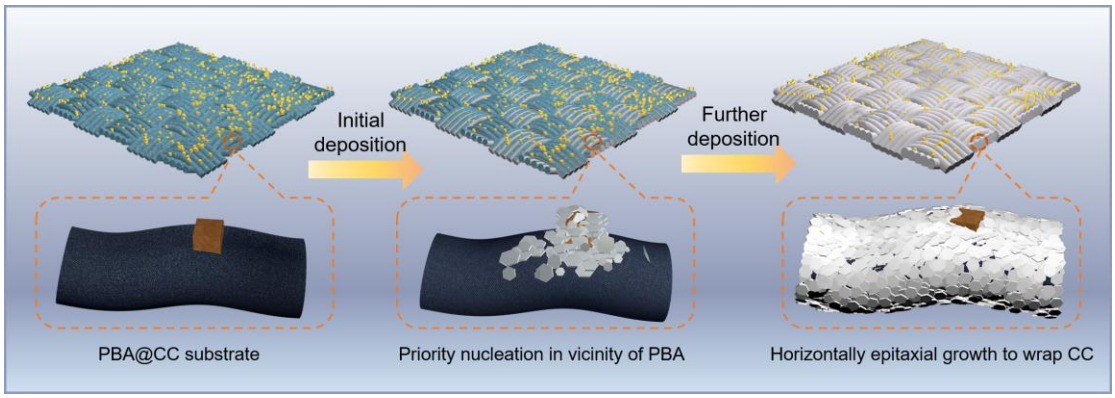

Fig. S25 Schematic diagram of deposition process during electrochemical processes on PBA@CC substrate.

The initial Zn plating on the PBA@CC substrate begins in the vicinity of the PBA crystals, probably because the Zn ion trapped in the framework of PBA provides the initial nuclei for Zn deposition. Previous reports generally believed that a uniform Zn nuclei layer on the entire substrate is required to ensure dendrite-free horizontal growth during deposition. However, the nonuniform nucleation process of zinc on PBA@CC substrates does not affect the subsequent planar growth and dense deposition of Zn, providing a unique example against the classical design principle of horizontally arranged zinc anodes. As Zn deposits to 2 mAh cm^{-2}, the nano crystals grow laterally and epitaxial growth along the carbon cloth surface to form a compact and uniform Zn layer. The PBA cubes remain stable and merge into the compact Zn layer.

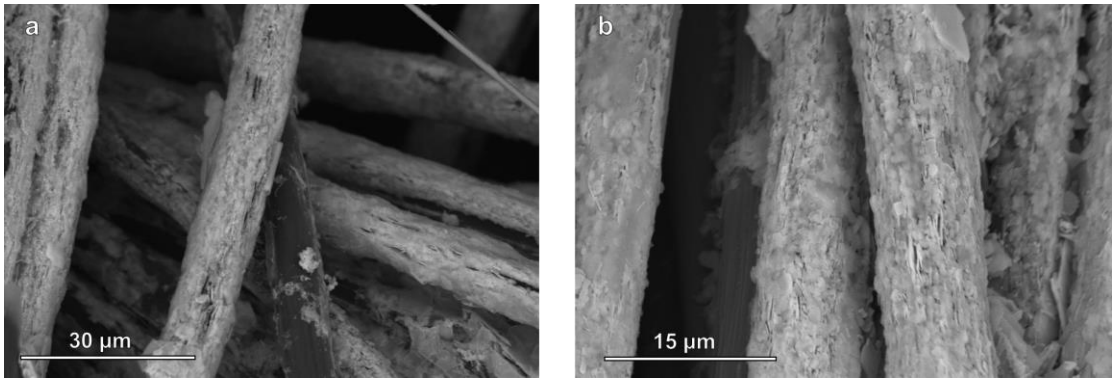

Fig. S26 (a, b) SEM images of ZnFe-PBA@CC after depositing with 2 mAh cm^{-2} capacities.

The horizontally arranged Zn deposition is highly homogeneous throughout a submillimetre region, without any detectable indications of aggressive dendritic growth.

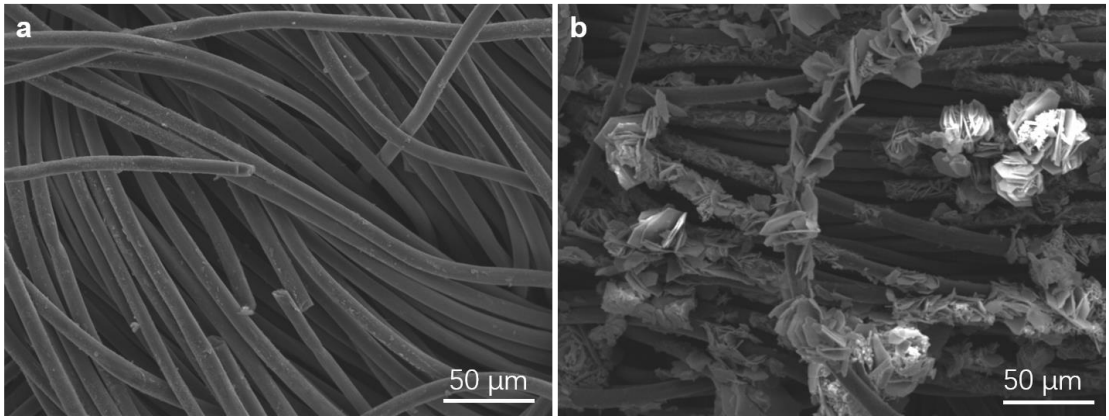

Fig. S27 SEM images of the 50th cycle after stripping of (a) ZnFe-PBA@CC and (b) CC substrates in 2.0 M $ZnSO_4$.

A considerable portion of the Coulombic inefficiency of Zn plating/stripping comes from the isolated ‘dead’ Zn that only partially dissolve during subsequent cycles. The PBA@CC substrate enables complete zinc dissociation after 50 cycles, with almost no residual zinc on the smooth CC fibre. In contrast, the CC substrate resides with ‘dead’ Zn that cannot be dissociated in the charged state, which comes from the accumulation of irreversible capacity during cycles.

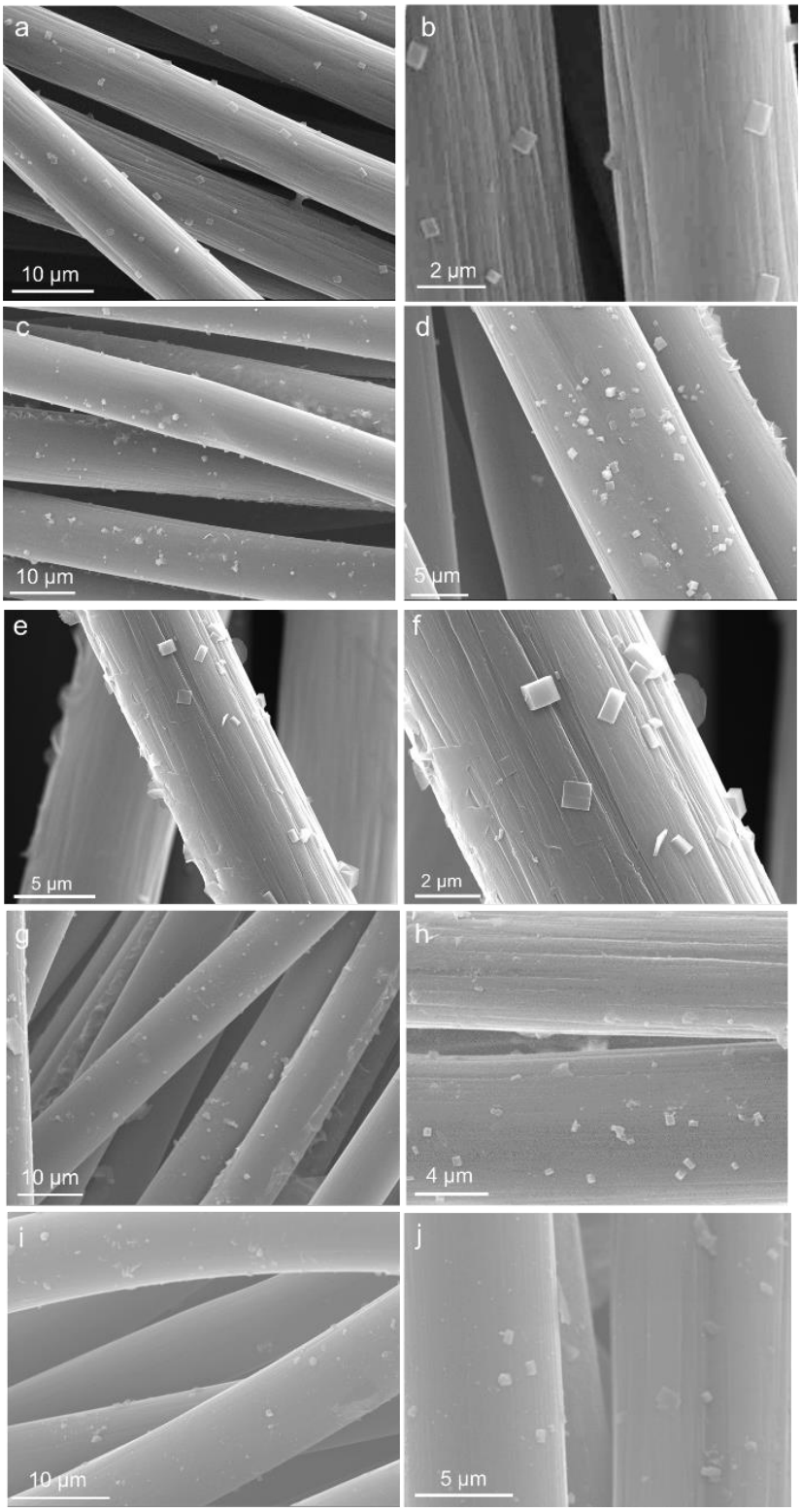

Fig. S28 SEM images of the ZnFe-PBA@CC substrates after the (a, b) pristine, (c, d) 100th, (e, f) 200th, (g, h) 300th and (i, j) 500th Zn plating/stripping cycles at 0.5 mA cm^{-2} and 0.5 mAh cm^{-2}.

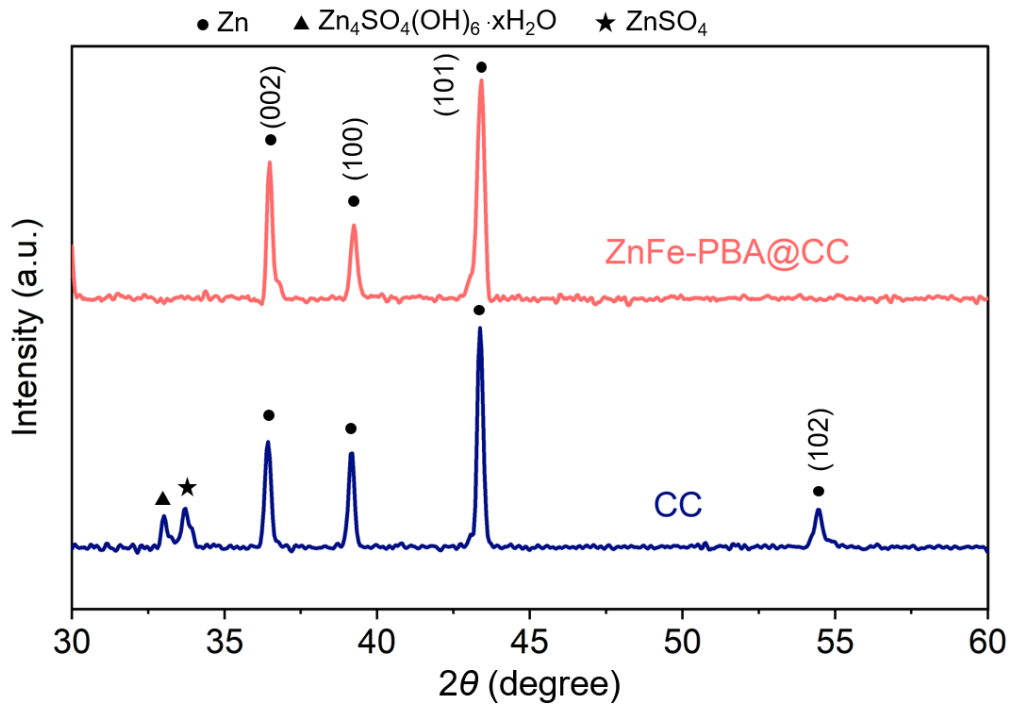

Fig. S29 XRD of ZnFe-PBA@CC and CC after depositing 0.5 mAh cm^{-2} in 13.0 M $ZnCl_2$ electrolyte.

The Zn (002) plane located at 2θ = 36.3° shows higher intensity for Zn deposited on PBA@CC. The high I(002)/I(100) indicates the preferred deposition of Zn (002) plane.

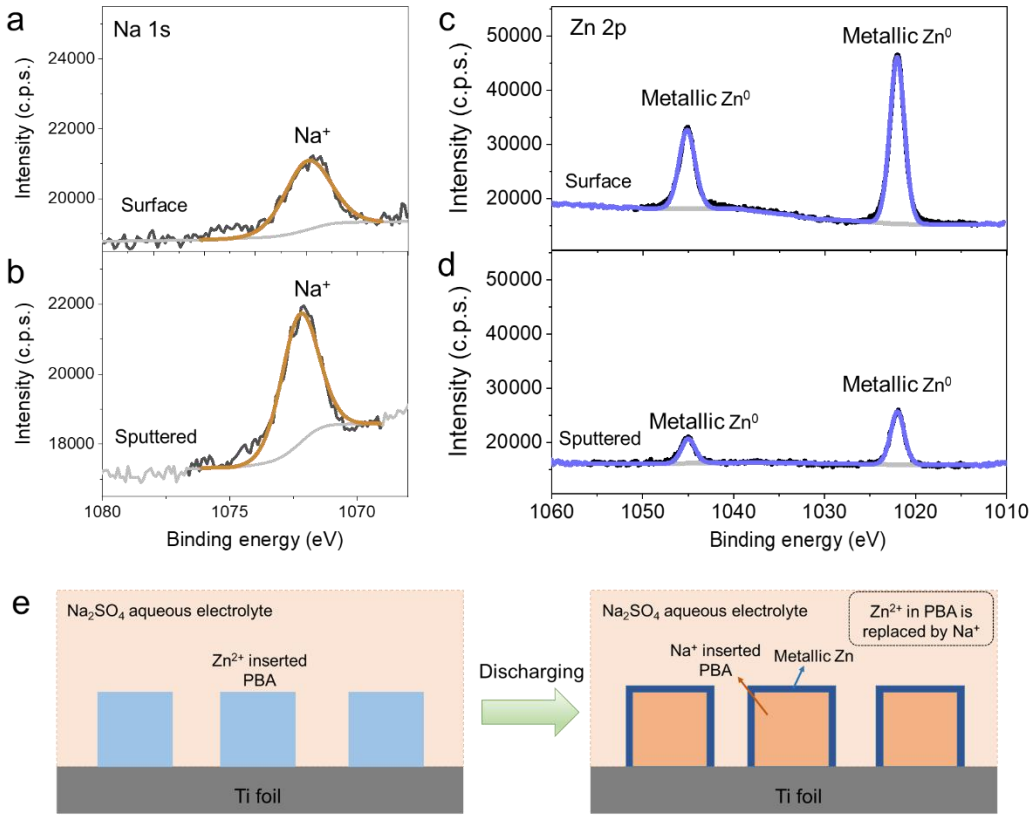

Fig. S30 The dynamical replacement for metal ions in PBA nanocavities. (a-d) XPS spectra of Na 1s (a, b) and Zn 2p (c, d) for a Zn-inserted NiFe-PBA substrate discharged in Na_2SO_4 solution. Upper panels and lower panels show spectra before and after Ar^+ sputtering, respectively. (e) Schematic of dynamical ion replacement.

A zinc-inserted NiFe-PBA@CC substrate was discharged at 0.5 mA cm^{-2} in 0.5 M Na_2SO_4 electrolyte for 1 h. The signal of zerovalent Zn is strong on the surface while become weak after 200s Ar^+ sputtering, during which the material on the sample surface was etched away (Fig. S30). In contrast, the signal of Na^+ increases after sputtering, indicating a process of dynamical ion replacement (Zn^{2+} replaced by Na^+) shown in Fig. S30 d. It is worth noting that no signals of divalent zinc ions were observed in Zn 2p spectra either before or after Ar^+ sputtering, suggesting that the Zn^{2+} in the nanocavities can be migrate to the surface of PBA and reduced to zinc metal. That is, Zn^{2+} can be replaced and the empty nanocavities were occupied by the following inserted Na^+ ions. For comparison, Fig. S31 a-b show the XPS measurements of a zinc-inserted NiFe-PBA@CC substrate discharged in 1 M $ZnSO_4$ electrolyte. The coexistence of Zn metal and Zn^{2+} after Ar^+ sputtering suggests a dynamical ion replacement shown in Fig. S31 c.

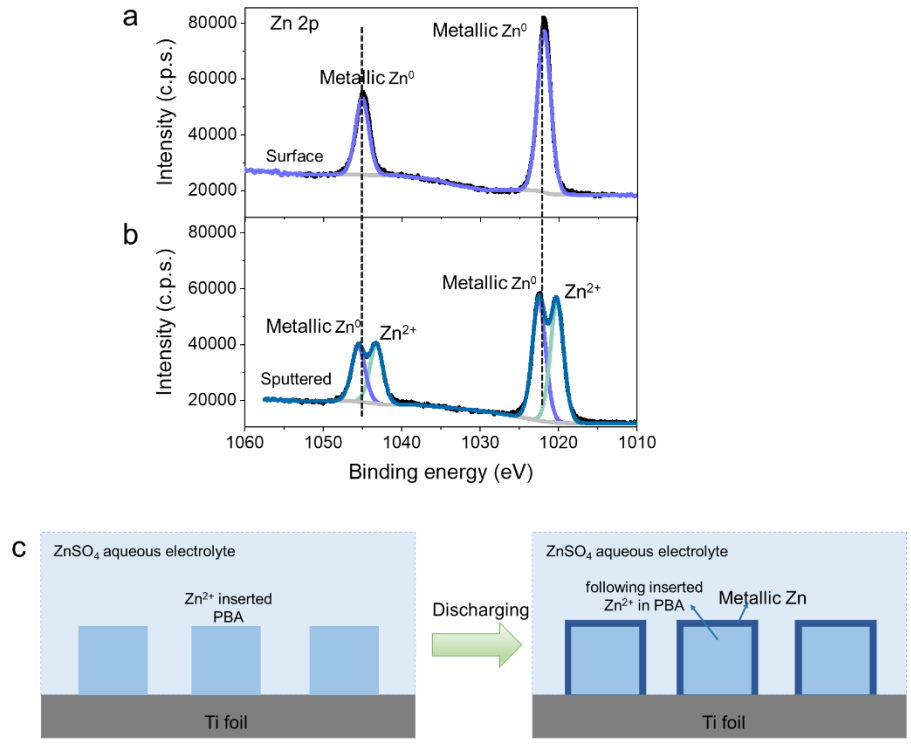

Fig. S31 The dynamical replacement for metal ions in PBA nanocavities. (a-b) XPS spectra of Zn 2p (c, d) for a Zn-inserted NiFe-PBA substrate discharged in $ZnSO_4$ solution. Upper panels and lower panels show spectra before and after Ar+ sputtering, respectively. (e) Schematic of dynamical ion replacement.

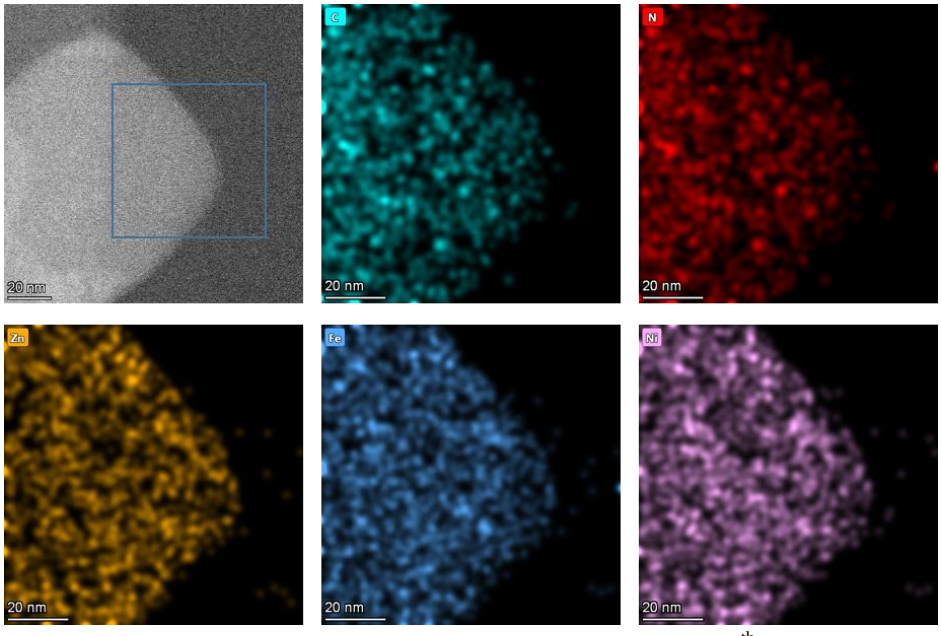

Fig. S32 HR-TEM and EDS mapping images of NiFe-PBA@CC after 10th Zn stripping.

After discharging, there is a large amount of uniformly distributed zinc elements in the PBA framework, which proves that the zinc ions remain stable in the nanocavities of the PBA after discharging.

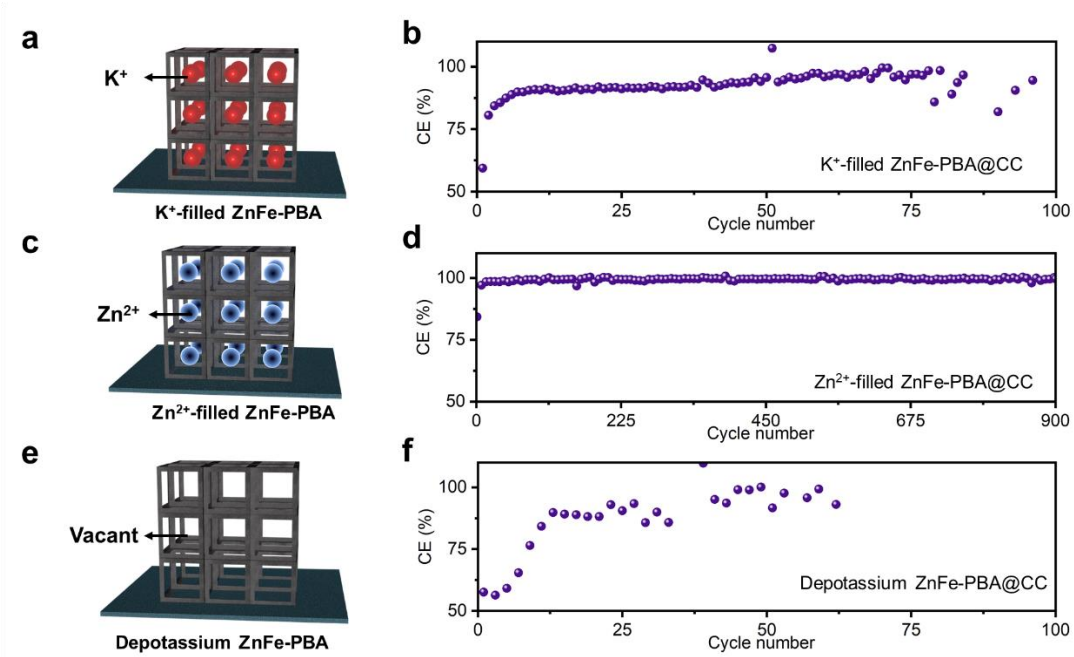

Fig. S33 (a) Schematic illustration and (b) CE evolution of K^+-filled ZnFe-PBA@CC substrate. (c) Schematic illustration and (d) CE evolution of Zn^{2+}-filled ZnFe-PBA@CC substrate. (e) Schematic illustration and (f) CE evolution of depotassium ZnFe-PBA@CC substrate.

We found that Zn^{2+} in the PBA nanocavities plays an important role for enhancing the plating/striping reversibility of PBA@CC substrate. The plating and stripping reversibility of the K^+-filled PBA@CC is higher than that of CC substrate, delivering a higher average CE and longer lifespan. However, the K^+ filled ZnFe-PBA@CC substrate possess a less reversible and unstable Zn plating/striping behavior compared to Zn^{2+} filled PBA@CC sample, especially in the initial 50 cycles. The CE of K^+ filled ZnFe-PBA@CC substrate tardily increases from 59% to 94% in the initial 50 cycles and finally stabilizes at >98% for 90 cycles at 0.5 mA cm^{-2} and 0.5 mAh cm^{-2}. This sluggish activation process, which is absence in Zn^{2+} filled PBA@CC, suggests the important role of zinc ions in the PBA framework for enhancing the reversibility of Zn plating/striping.

If the PBA frameworks have not experiment zinc ions insertion before the initial Zn deposition, the tunnel matrix loses its effect on the optimization of zinc anode reversibility. This indicates that the PBA framework itself is not possess a significant regulatory effect on zinc deposition. The ion channel matrix can only be brought into play when a large number of zinc ions are present inside the framework. In other words, the zinc trapping-plating process on lateral sides of PBA nanocubes relies on the presence of sufficient zinc ions in the initial PBA frameworks.

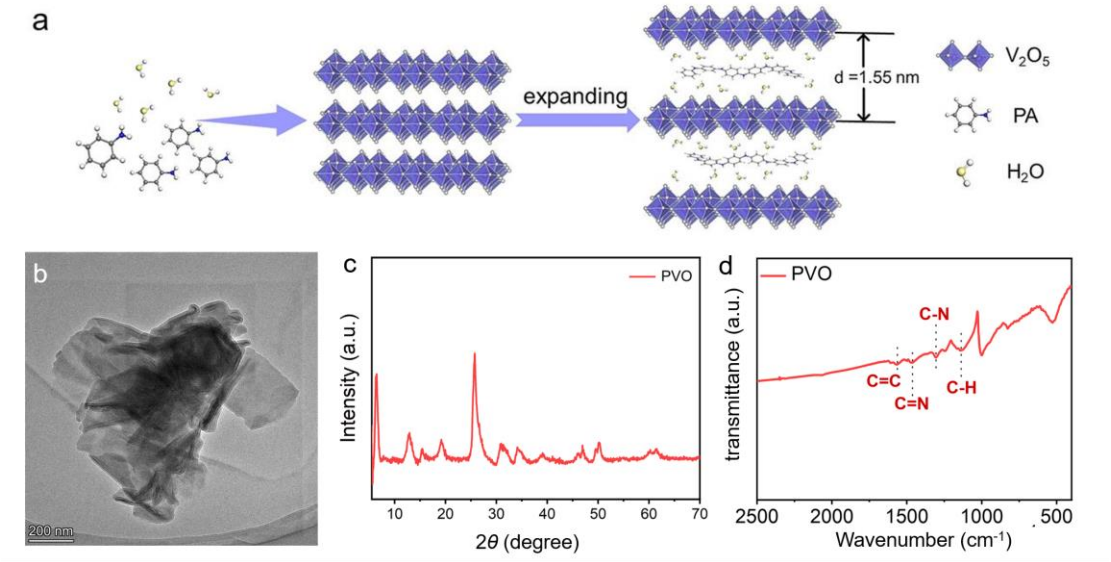

Fig. S34 (a) Illustration of the synthesis process for PVO. (b) TEM image of PVO. (c) XRD patterns and (d) FTIR patterns of PVO.

A 1.55 nm-interlayer spacing-expanded polyaniline-intercalated vanadium oxide (PVO) was choosed as the material for high ZUR zinc ion batteries. PVO was gained through a one-step hydrothermal method to intercalate PANI into the vanadium oxide layers. According to the TEM images, the microscopic morphology of PVO is layers of stacked nanosheets, XRD and FTIR results confirm the phase composition.

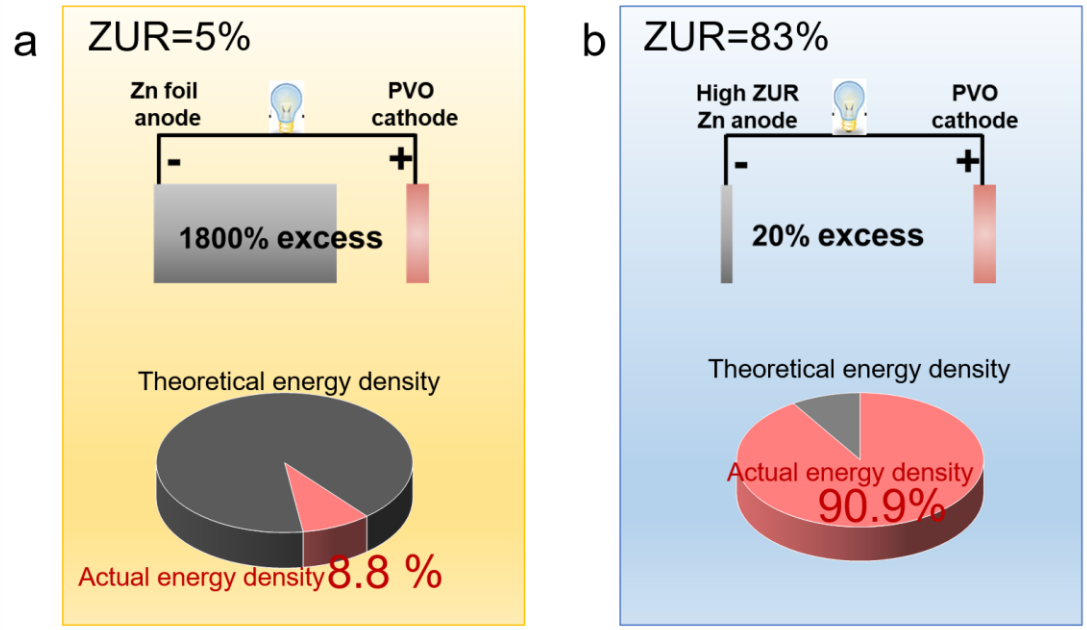

Fig. S35 Configuration of the anode and utilization ratio of the theoretical energy density of the conventional Zn foil-based battery and anode-limited Zn metal battery with 83% ZUR.

The key issue of current Zn metal battery research is that thick Zn sheets have been overwhelmingly tested; these sheets show low ZURs (generally less than 5%) and have an imbalanced anode-cathode configuration. The nearly unlimited zinc reservoir potentially favours enhanced cycling stability in the laboratory but severely limits the actual energy density of full batteries. ZUR is an important metric for determining how much of the promised high energy density of aqueous Zn based cells can be realized at the device level. As illustrated by Fig. 6b, the Zn foil with low ZUR (less than 5%) presents at least 1800% over-provision of Zn anodes, resulting in that Zn foil//PVO configuration can only fulfill 8.8% of theoretical energy density. The PBA@CC architecture optimizes the N/P ratio and implements only a 20% Zn excess in the battery construction, which realize 90.9% of the promised energy density of the full cell via lowering the anode weight.

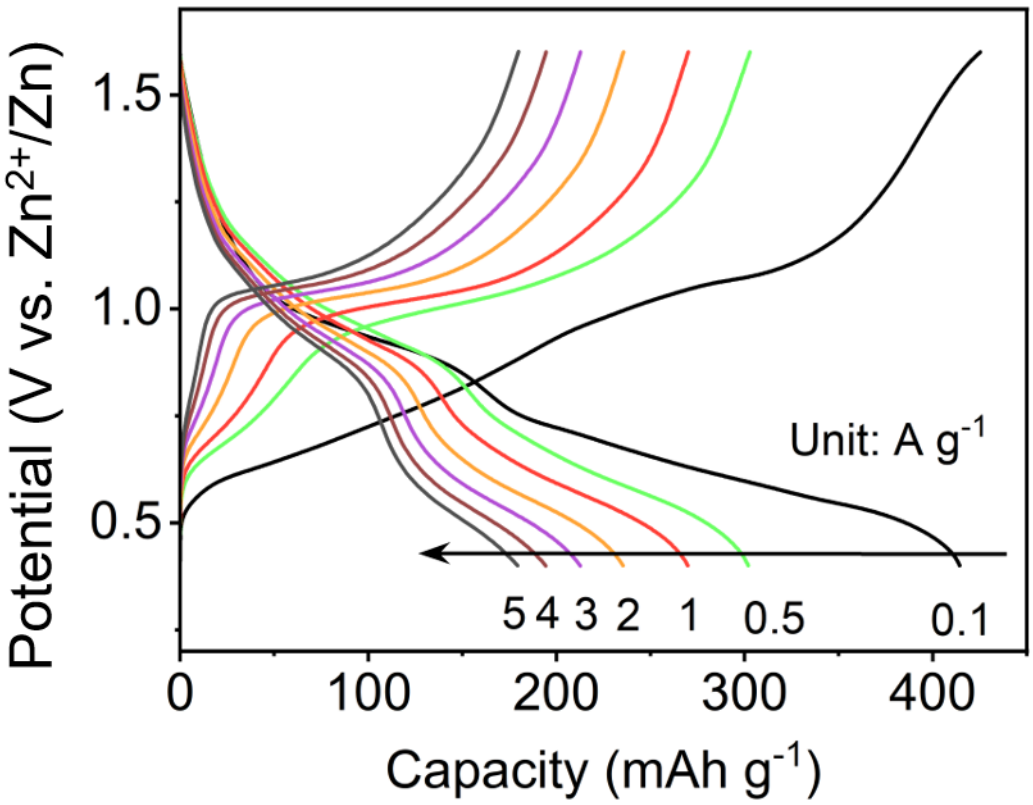

Fig. S36 Galvanostatic charge/discharge curves of PVO// ZnFe-PBA@CC full battery at diffident current densities.

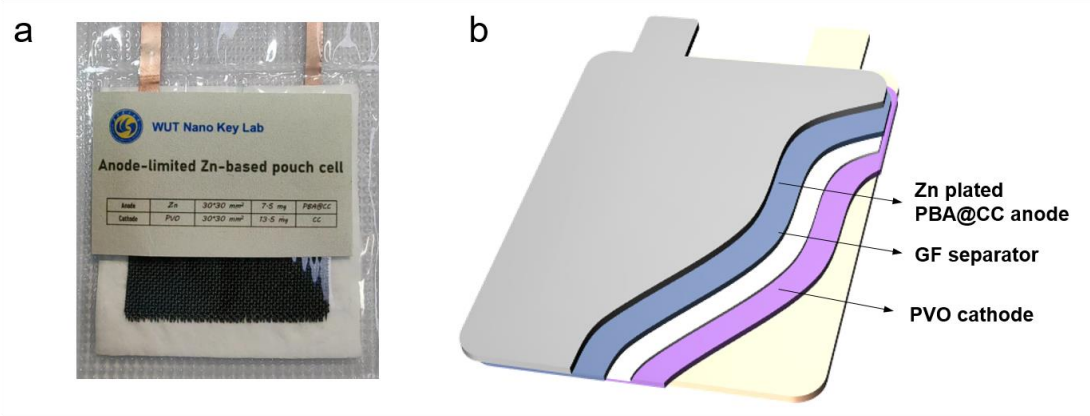

Fig. S37 Photo and Schematic of the anode-limited pouch cell.

References

[1] J. X. Zheng, Q. Zhao, T. Tang, J. F. Yin, C. D. Quilty, G. D. Renderos, X. T. Liu, Y. Deng, L. Wang, D. C. Bock, C. Jaye, D. H. Zhang, E. S. Takeuchi, K. J. Takeuchi, A. C. Marschilok, L. A. Archer, *Science* **2019**, *366*, 645.

[2] Y. P. Zhu, Y. Cui, H. N. Alshareef, *Nano Lett.* **2021**, *21*, 1446.

[3] Z. H. Yi, J. X. Liu, S. D. Tan, Z. Y. Sang, J. Mao, L. C. Yin, X. G. Liu, L. Q. Wang, F. Hou, S. X. Dou, H. M. Cheng, J. Liang, *Adv. Mater.* **2022**, *34*.

[4] H. Meng, Q. Ran, T.-Y. Dai, H. Shi, S.-P. Zeng, Y.-F. Zhu, Z. Wen, W. Zhang, X.-Y. Lang, W.-T. Zheng, Q. Jiang, *Nanomicro Lett.* **2022**, *14*, 128.

[5] Z. Wang, J. H. Huang, Z. W. Guo, X. L. Dong, Y. Liu, Y. G. Wang, Y. Y. Xia, *Joule* **2019**, *3*, 1289.

[6] X. Zheng, Z. Liu, J. Sun, R. Luo, K. Xu, M. Si, J. Kang, Y. Yuan, S. Liu, T. Ahmad, T. Jiang, N. Chen, M. Wang, Y. Xu, M. Chuai, Z. Zhu, Q. Peng, Y. Meng, K. Zhang, W. Wang, W. Chen, *Nat. Commun.* **2023**, *14*, 76.

[7] K. Xu, *Commun. Mater.* **2022**, *3*, 31.